INSTITUTE OF PHYSICS PUBLISHING PHYSIOLOGICAL MEASUREMENT

Physiol. Meas. **26** (2005) S185–S197 doi:10.1088/0967-3334/26/2/018

Excitation patterns in three-dimensional electrical impedance tomography

Hamid Dehghani, Nirmal Soni, Ryan Halter, Alex Hartov and Keith D Paulsen

Thayer School of Engineering, Dartmouth College, Hanover, NH 03755, USA

Received 1 September 2004, accepted for publication 26 October 2004
Published 29 March 2005
Online at stacks.iop.org/PM/26/S185

Abstract

Electrical impedance tomography (EIT) is a non-invasive technique that aims to reconstruct images of internal electrical properties of a domain, based on electrical measurements on the periphery. Improvements in instrumentation and numerical modeling have led to three-dimensional (3D) imaging. The availability of 3D modeling and imaging raises the question of identifying the best possible excitation patterns that will yield to data, which can be used to produce the best image reconstruction of internal properties. In this work, we describe our 3D finite element model of EIT. Through singular value decomposition as well as examples of reconstructed images, we show that for a homogenous female breast model with four layers of electrodes, a driving pattern where each excitation plane is a sinusoidal pattern out-of-phase with its neighboring plane produces better qualitative images. However, in terms of quantitative imaging an excitation pattern where all electrode layers are in phase produces better results.

Keywords: impedance tomography, finite element modeling, image reconstruction

(Some figures in this article are in colour only in the electronic version)

1. Introduction

Electrical impedance tomography (EIT) is a method that aims to reconstruct images of internal electrical property (conductivity, permittivity and permeability in some high-frequency non-medical applications) distributions from electrical measurements obtained on the periphery. In recent years EIT has been the subject of study for a variety of clinical problems such as lung ventilation (Adler *et al* 1997, Brown *et al* 1994, Frerichs 2000, Metherall *et al* 1996, Noble *et al* 1999, Woo *et al* 1992, Valente Barbas 2003, Newell *et al* 1993, van Genderingen *et al* 2004, 2003), cardiac volume changes (Hoetink *et al* 2001,

Brown *et al* 1992, Vonk Noordegraaf *et al* 1997), gastric emptying (Erol *et al* 1996), head imaging (Holder 1992, Bagshaw *et al* 2003) and breast cancer detection (Cherepenin *et al* 2003, Kerner *et al* 2002, Wang *et al* 2001, Zou and Guo 2003).

In EIT, measurements over a region of interest are acquired from a set of electrodes by applying currents and measuring resulting voltages or vice versa. Depending on the application, various driving schemes have been used for electrode excitation, including stimulation of adjacent and opposite pairs or trigonometric spatial patterns (Boone *et al* 1997, Lionheart 2004, Brown 2003). Once boundary measurements are acquired, estimates of the electrical property distributions in tissue can be determined through the appropriate model-based matching of the data.

The majority of modeling and image reconstruction studies have involved two-dimensional (2D) assumptions; yet, a three-dimensional (3D) treatment of electrical transmission in tissue provides a more accurate prediction of the field distribution in the medium. Recently, there has been significant progress in developing 3D modeling and image reconstruction which is computationally more complex but also more accurate (Metherall *et al* 1996, Goble 1990, Molinari *et al* 2002, Polydorides and Lionheart 2002, Vauhkonen *et al* 1999). As 3D image reconstruction becomes more fully developed it is crucial to define the appropriate excitation (drive) patterns that will provide the maximum information on the internal properties of the domain being imaged. This is particularly true when using experimental patient data, since theoretical simulations will typically not represent the level of noise and systematic error present in actual data sets and simple symmetrical geometries no longer apply. Some results have appeared in this regard, notably the work by Goble (1990), who extended the original distinguishability of Isaacson (1986). This work showed that the eigenfunctions for a finite 3D cylinder constitute an optimal drive pattern set on discrete electrodes.

In the presented paper, we describe our implementation of a 3D finite element model (FEM) for EIT. In section 2, we describe our implementation of the FEM for EIT in some detail to accurately describe the software used for the presented study. We use simulation studies coupled to singular value decomposition (SVD) of the data to evaluate the performance of various excitation patterns for a homogenous female breast model that contains 64 electrodes distributed over 4 planes of 16 electrodes each. We validate these findings by reconstructing images from simulated data. We show that for a homogenous female breast model with four layers of electrodes, a driving pattern where each excitation plane is a sinusoidal pattern, which is out-of-phase with its neighboring planes, produces better qualitative images. However, in terms of quantitative imaging an excitation pattern where all electrode layers are in phase produces the best results.

2. Theory

Under certain low-frequency assumptions, it is well established that the full Maxwell equations can be simplified to the complex-valued Laplace equation

$$\nabla \cdot \sigma^* \nabla \Phi^* = 0 \tag{1}$$

where Φ^* is the complex-valued electric potential and σ^* is the complex conductivity of the medium ($\sigma^* = \sigma - \mathrm{i}\omega\varepsilon_\mathrm{o}\varepsilon_\mathrm{r}$, for ω is the frequency, ε_o and ε_r are the absolute and relative permittivities). In order to obtain a reasonable model for EIT, appropriate boundary conditions need to be enforced (Vauhkonen 1997). In this work we use the complete electrode model, which takes into account both the shunting effect of the electrodes and the contact impedance

between the electrodes and tissue. Using this boundary condition the EIT model includes (Vauhkonen 1997)

$$\Phi^* + z_l \sigma^* \frac{\partial \Phi^*}{\mathrm{d}n} = V_l^*, \qquad x \in e_l, \quad l = 1, 2, \ldots, L \tag{2}$$

$$\int_{e_l} \sigma^* \frac{\partial \Phi^*}{\mathrm{d}n} \, \mathrm{d}S = I_l^*, \qquad x \in e_l, \quad l = 1, 2, \ldots, L \tag{3}$$

$$\sigma^* \frac{\partial \Phi^*}{\mathrm{d}n} = 0, \qquad x \in \partial\Omega \Big/ \cup_l^L e_l \tag{4}$$

where z_l is the effective contact impedance between the lth electrode and the tissue, n is the outward normal, V^* is the complex-valued voltage, I^* is the complex-valued current and e_l denotes the electrode l. $x \in \partial\Omega \Big/ \cup_l^L e_l$ indicates a point on the boundary not under the electrodes.

2.1. Finite element implementation

The finite element discretization of a domain Ω can be obtained by subdividing it into D elements joined at V vertex nodes. In finite element formalism, $\Phi(\mathbf{r})$ at spatial point r is approximated by a piecewise continuous polynomial function $\Phi^h(r, w) = \sum_i^V \Phi_i(w) u_i(r) \in \Omega^h$, where Ω^h is a finite-dimensional subspace spanned by basis functions $\{u_i(r); i = 1, \ldots, V\}$ chosen to have limited support. The problem of solving for Φ^h becomes one of sparse matrix inversion: in this work, we use a bi-conjugate gradient stabilized solver. Equation (1) in the FEM framework can be expressed as a system of linear algebraic equations:

$$(K(\sigma^*) + z^{-1} F)\Phi^* = 0 \tag{5}$$

where the matrices $K(\sigma^*)$ and F have entries given by:

$$K_{ij} = \int_\Omega \sigma^*(r) \nabla u_i(r) \cdot \nabla u_j(r) \, \mathrm{d}^n r \tag{6}$$

$$F_{ij} = \oint_{\partial\Omega \in l} u_i(r) u_j(r) \, \mathrm{d}^{n-1} r \tag{7}$$

where $\delta\Omega \in l$ is the boundary under each electrode.

2.2. Image reconstruction

In the inverse (imaging) problem, the goal is the recovery of σ^* at each FEM node based on measurements at the object surface. Here, we aim to recover internal electrical property distributions from the boundary measurements. We assume that σ and ε_r are expressed in a piecewise linear basis with a limited number of dimensions (less than the dimension of the finite element system matrices). A number of different strategies for defining the reconstruction basis are possible; in this paper we use a linear pixel basis of dimensions $30 \times 30 \times 10$ (x, y and z), which spans the whole domain.

Image reconstruction is achieved numerically by minimizing an objective function, which depends on the difference between measured data, Φ^{M^*}, and calculated data, Φ^{C^*}, from the FEM solution to equation (1) under the assumptions of the present iteration property estimate. Typically this is written as the minimization of χ^2:

$$\chi^2 = \sum_{i=1}^{NM} \left| \Phi_i^{M^*} - \Phi_i^{C^*} \right|^2 \tag{8}$$

where NM is the number of measurements and || indicates the magnitude of the difference vector of a complex number which in the complex plane is formed by multiplying the difference vector by its complex conjugate transpose to produce a real-valued scalar. χ^2 can be minimized in a least-squares sense by setting its derivatives with respect to the electrical distribution parameter equal to zero, and solving the resultant nonlinear system using a Newton–Raphson approach. We use a Levenberg–Marquardt algorithm, to repeatedly solve

$$a = J^T(JJ^T + \lambda I)^{-1}b \tag{9}$$

where b is the data vector, $b = (\Phi^{M^*} - \Phi^{C^*})^T$; a is the solution update vector, $a = \delta[\sigma + i\omega\varepsilon_o\varepsilon_r]$, defining the difference between the true and estimated electrical properties at each reconstructed basis. λ is the regularization factor to stabilize matrix inversion; J is the Jacobian matrix for our model, which is calculated using the so-called adjoint method (Polydorides and Lionheart 2002). It has the form

$$J = \begin{bmatrix} \frac{\delta\Phi_1^*}{\delta\sigma_1^*} & \frac{\delta\Phi_1^*}{\delta\sigma_2^*} & \cdots & \frac{\delta\Phi_1^*}{\delta\sigma_j^*} \\ \frac{\delta\Phi_2^*}{\delta\sigma_1^*} & \frac{\delta\Phi_2^*}{\delta\sigma_2^*} & \cdots & \frac{\delta\Phi_2^*}{\delta\sigma_j^*} \\ \vdots & \vdots & \ddots & \vdots \\ \frac{\delta\Phi_n^*}{\delta\sigma_1^*} & \frac{\delta\Phi_n^*}{\delta\sigma_2^*} & \cdots & \frac{\delta\Phi_n^*}{\delta\sigma_j^*} \end{bmatrix} \tag{10}$$

where $\frac{\delta\Phi_n^*}{\delta\sigma_j^*}$ are the sub-matrices that define the derivative relation between the nth measurement with respect to σ^* at the jth reconstructed node. It may be worth noting that equation (9) is the under-determined equivalent of the more generally used over-determined problem, i.e. $a = (J^TJ + \lambda I)^{-1}J^Tb$, where the size of the Hessian matrix (second derivative) JJ^T is n^2 as compared to J^TJ which has a size of j^2 (where j is the total number of nodes). Since, in most cases when $n \ll j$, it is computationally significant to use this scheme.

3. Methods

In order to evaluate the best excitation pattern options to use in a 3D imaging system, a realistic female breast model of dimensions 63.2 mm × 58.9 mm × 94.5 mm (x, y, z) was simulated (figure 1). The mesh consisted of 16 303 nodes corresponding to 66 151 linear tetrahedral elements. The resolution of the mesh was chosen such that the model is numerically accurate, as compared to a higher node density or higher order elements. Four planes of electrodes were modeled (at $z = -20$ mm, -40 mm, -60 mm and -80 mm) with each plane consisting of 16 circular electrodes of diameter 5 mm, and spaced vertically 20 mm apart. The model assumed homogenous electrical properties of $\sigma = 2$ Sm^{-1} and $\varepsilon_r = 80$. All of the data presented in this work were confined to an excitation frequency of 125 kHz.

In the first analysis, the 'voltage' drive mode was considered. Here, one applies a set of voltage patterns at each electrode simultaneously and measures the resulting currents at the same electrodes. Three voltage driving patterns were considered: (1) 15 sinusoidal voltage patterns distributed circumferentially in the plane and in-phase between all four planes, (2) 15 sinusoidal voltage patterns distributed circumferentially within each plane but 45° out-of-phase with respect to neighboring planes, and (3) 15 sinusoidal voltage patterns distributed circumferentially within each plane but 90° out-of-phase with respect to neighboring planes. In each case, the Jacobian was calculated and used to evaluate the amount of information available for each set of current patterns. Singular value decomposition of the Jacobian matrix

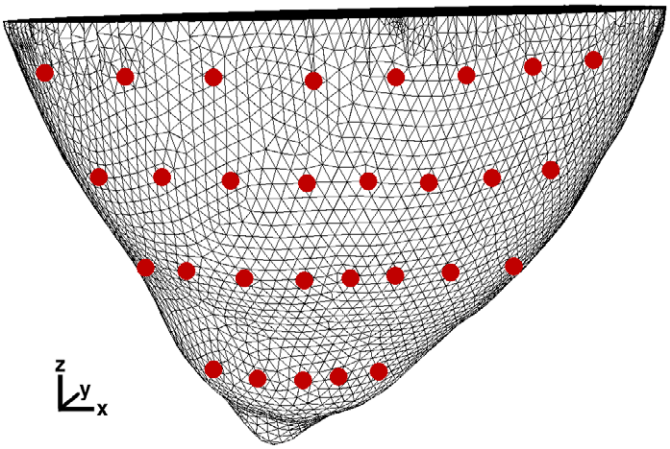

Figure 1. Finite element model used for the generation of the Jacobian and simulated forward data. The mesh is a realistic female breast model of dimensions 63.2 mm × 58.9 mm × 94.5 mm (x, y, z). Four planes of electrodes (represented by shaded circles) are also modeled. Each plane contains 16 equally spaced circular electrodes of radius 5 mm, at $z = -20$, -40, -60 and -80 mm.

yields a triplet of matrices:

$$J = USV^T \tag{11}$$

where U and V are orthonormal matrices containing the singular vectors of J and S is a diagonal matrix containing the singular values of J. Since J serves to map measurements onto electrical properties, it can be viewed as an interface between the detection space and the image space. Furthermore, the vectors of U and V correspond to the modes in detection space and image space, respectively, while the magnitude of the singular values in S represents the importance of the corresponding singular vectors in U and V. Specifically, more nonzero singular values mean more modes are active in the two spaces which brings more detail and improves the resolution in the resultant image. In a practical setup, noise must be considered because only the singular values larger than the noise level provide useful information. The singular values of the sensitivity maps for the whole domain are calculated. There are normally M nonzero singular values in the diagonal matrix when N (number of nodes) is larger than M (number of measurements) and those values are sorted in descending order. Thus, it is possible to determine whether a given set of excitation patterns provides more information about the domain under investigation relative to other pattern options.

In order to evaluate further the suitability of one excitation pattern over another, boundary data were calculated for each set of excitation patterns in the presence of two anomalies: a single spherical conductor (5 times the background value, radius 10 mm, located at mid-plane, 20 mm from center) and a single spherical permittivity anomaly (10 times the background value, radius 10 mm, located at mid-plane, 20 mm from center) (figure 2). Using these data sets, images were reconstructed using a linear pixel scheme. For image reconstruction, the initial value of regularization was chosen to be 1×10^{-5}. At each iteration, if the projection error, χ^2, was found to have decreased as compared to the previous iteration, regularization was decreased by a factor of $10^{1/8}$. All images shown are those chosen when the projection error χ^2 did not decrease by more than 1% as compared to the previous iteration.

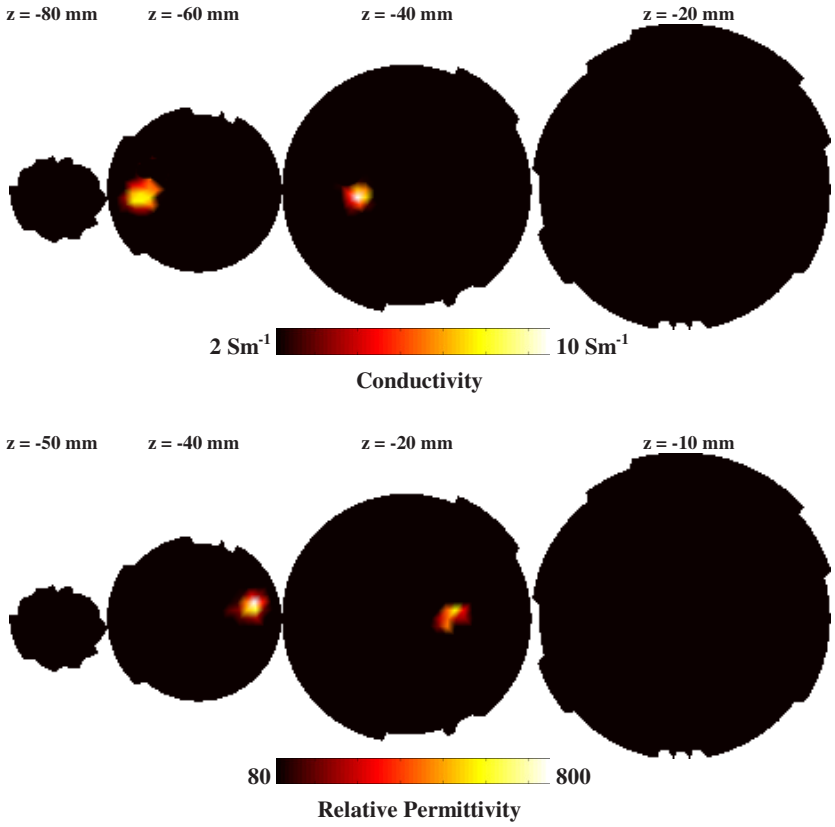

Figure 2. 2D coronal slices through the breast mesh showing the position of the anomalies. The most right-hand slice is near the chest while the most left-hand slice is near the nipple.

4. Results

Singular values of each Jacobian were calculated for each excitation pattern and the normalized values (normalized to the first and largest singular value) are plotted in figure 3. It is evident from this plot that the second and third excitation patterns, where the applied voltage at each plane is out-of-phase with the other planes, provide more information than the first pattern. The total number of singular values is 960 (15 excitation patterns times 64 measurements), and if one takes into account the expected noise in the measurement system it is possible to calculate the total number of useful singular values (proportional to the amount of useful information) for each pattern. Assuming that the noise in the measured data from a clinical instrument is about 0.1%, the total number of useful singular values is: 269 for the first pattern, 329 for the second pattern and 330 for the third pattern. This suggests that using out-of-phase patterns at each level produces better reconstructed images of the domains internal electrical properties from the measured data.

Reconstructed images from the simulated data in the presence of anomalies within the domain (figure 2) are shown in figures 4–6, using the first, second and third patterns, respectively. Both the conductivity and permitivity anomalies have been recovered for all excitation patterns, at approximately the correct location and with good separation. These are the images at the fifth iteration, which were obtained with a computation time of approximately

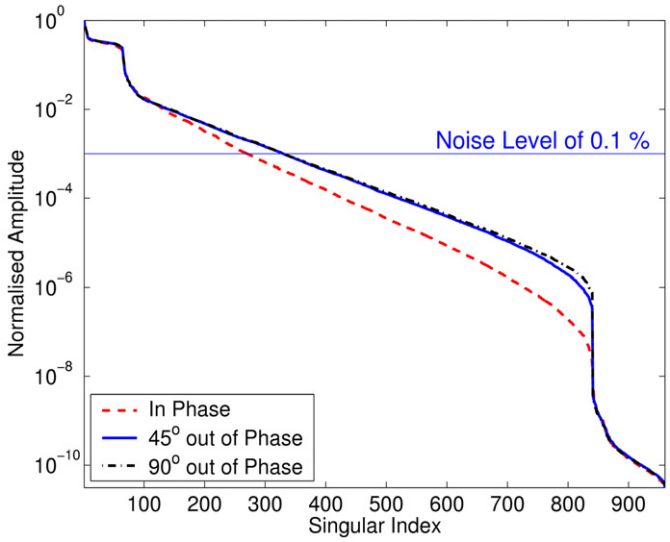

Figure 3. Singular values of each Jacobian calculated using the three different applied patterns. Each set of singular values is normalized with respect to the first and largest singular value. The solid horizontal line represents the cut-off level when 0.1% noise is expected in the data.

Table 1. The target and the calculated volume of each reconstructed anomaly.

	Target	Pattern 1	Pattern 2	Pattern 3
Conductivity volume (mm^3)	4.2×10^3	23×10^3	15×10^3	13×10^3
Permittivity volume (mm^3)	4×10^3	11×10^3	7.8×10^3	7.7×10^3

10 min per iteration on a 1.7 GHz PC with 2 GB of RAM. It is evident that the recovered target values are much lower than expected, a problem that is commonly reported in 3D imaging with related modalities (Dehghani *et al* 2003, Gibson *et al* 2003). No doubt these quantitative values can be dramatically improved using different and more sophisticated regularization schemes as well as addition of appropriate penalty function (Borsic 2002).

In order to more clearly analyse the results, the total volume of each reconstructed anomaly has been calculated and displayed in table 1. The volumes were computed as the total volume of mesh elements with nodes having a reconstructed value of greater than the full width half maximum (FWHM) of the anomaly. It should be noted here that since the mesh is not regular the actual anomaly does not have a perfect spherical shape, which gives rise to the different volume estimated for the conductivity and permittivity objects.

Finally, in order to investigate the application of *a priori* information in image reconstruction, images were reconstructed using the known location of each anomaly in a parameter reduction (region basis) algorithm as outlined by Dehghani *et al* (2003). Briefly, images are reconstructed assuming correct knowledge of the location and size of the anomalies (potentially obtainable from other modalities). This information is then used to reduce the number of unknowns to three (background, and two anomalies) for image reconstruction. Reconstructed images using this algorithm and the first excitation pattern are shown in figure 7. All three excitation patterns produced the same reconstruction, but the first pattern

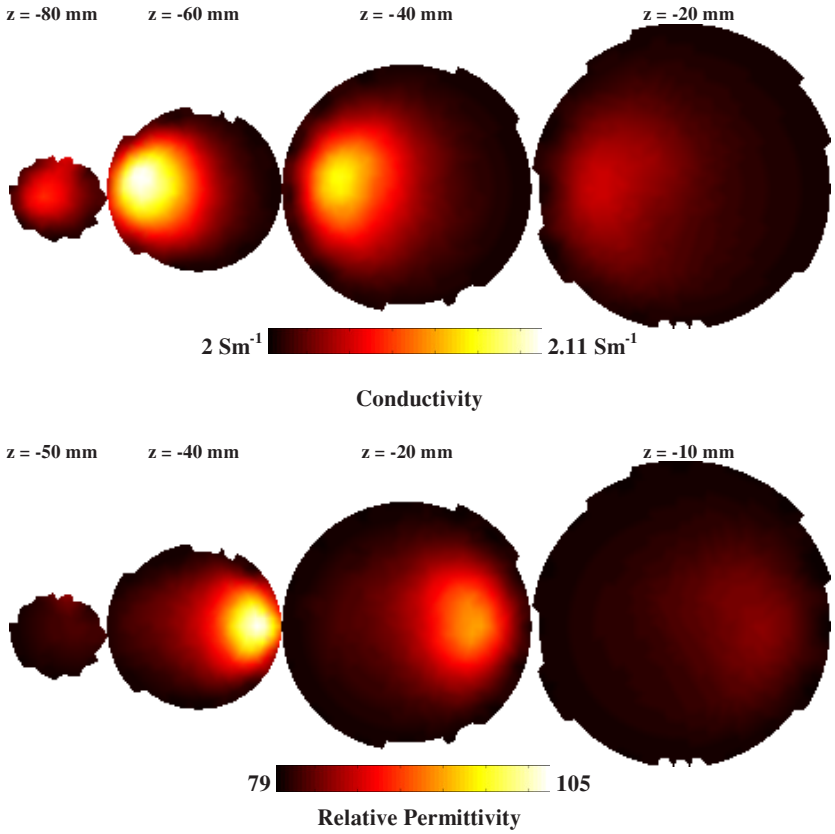

Figure 4. 2D coronal slices of the 3D reconstruction of internal conductivity and permittivity distributions using the first excitation pattern. The most right-hand slice is near the chest while the most left-hand slice is near the nipple.

iterated to a stable solution at iteration 13, whereas the second and third patterns stabilized by iteration 8.

5. Discussion

In this work, we have presented our implementation of a three-dimensional finite element model for electrical impedance imaging. We have used this model to investigate three-dimensional excitation patterns for a female breast model consisting of 4 levels of 16 electrodes. Specifically we have calculated the Jacobian (sensitivity map) for the whole model using each in-phase and out-of-phase drive pattern and performed singular value decomposition to examine the amount of information available from each drive pattern, which is above the noise floor of a typical measurement system. It has been shown that using an excitation pattern where each level of electrodes is excited with a sinusoidal pattern in the plane that is in-phase with all of the other planes contained the least amount of information about the imaging domain. By comparison, when the driving patterns for each plane of electrodes were out-of-phase with one another, there is a significant increase in the total number of singular values (figure 3), which occur above the noise threshold with the third pattern (each plane

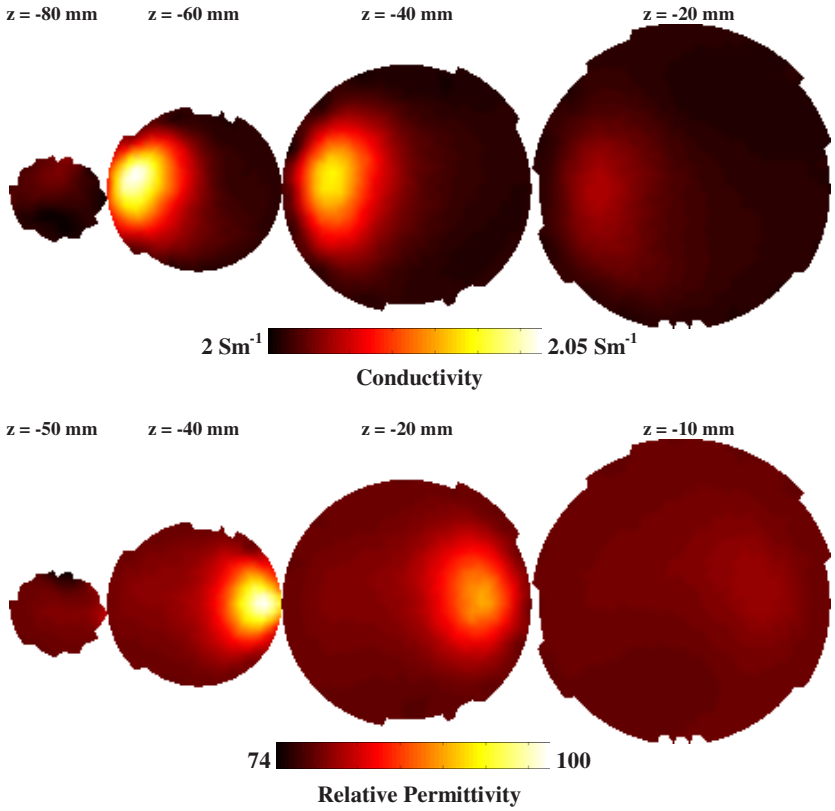

Figure 5. As in figure 4, but using the second drive pattern (45° out of phase).

being 90° out phase) producing the best results. The second and third patterns are such that they dictate a sinusoidal driving pattern, not only in the plane of the electrodes, but also in the z-direction. Other similar studies (Polydorides and McCann 2002) have used the SVD analysis as well as Picard plots to show how different electrode configuration can increase resolution in a 2D EIT problem. In their work they have shown that in an ill-posed problem where the measurements are contaminated with some noise, a stable solution exists if the Picard criterion is satisfied. According to these criteria, the Picard coefficients $\{U^T{}_i b\}$ should decay to zero faster than the (generalized) singular values, where U is the left orthogonal factor of J and b the measurements vector. The work presented, particularly the results shown in figure 3 where the number of useful singular values above the expected noise limits can also be expanded to show relevant Picard plots, but it is expected that identical results will be achieved; namely that more information regarding the domain being imaged can be obtained with a driving pattern where each plane is out-of-phase with another.

The increase in the total useful number of singular values for the out-of-phase driving pattern can be explained by considering the flow of current within the medium. For a driving pattern where all planes of excitation are of the same phase, the current will flow through the medium without being forced to sample the areas directly underneath and between the planes of each electrode. Whereas for the out-of-phase driving patterns, due to the potential difference between each electrode of different phase, the current is forced to sample the volume underneath and between each electrode plane as well as sampling deep within the medium,

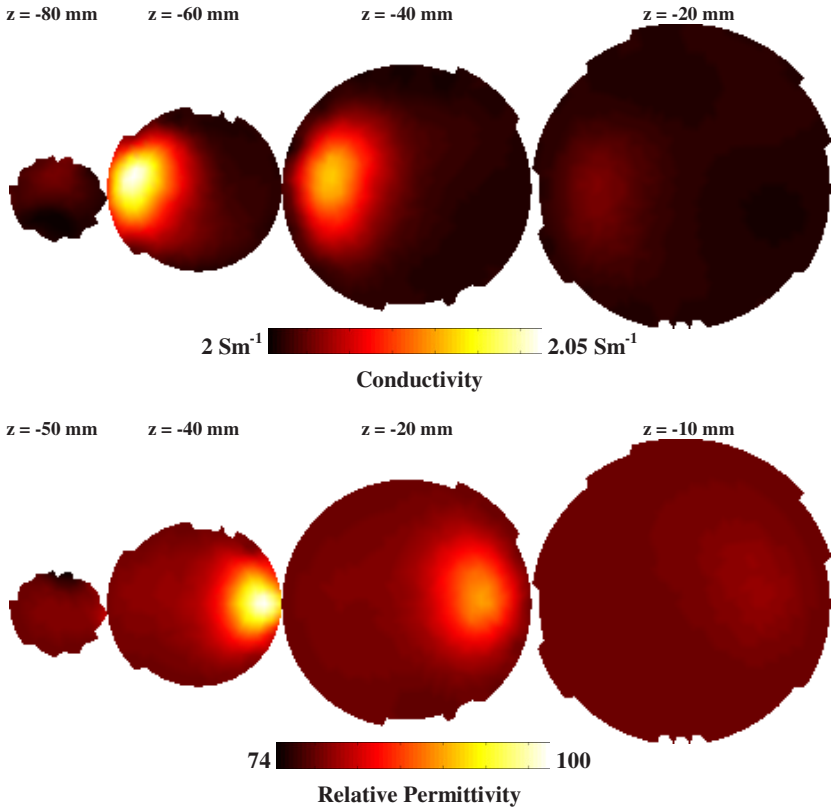

Figure 6. As in figure 4, but using the third drive pattern (90° out of phase).

at a cost of reduced sensitivity to these deeper regions. Therefore, since the out-of-phase driving patterns sample a larger area, the amount of information contained within them is increased. Finally it is very important to state that each of the 3 different current patterns does give rise to the same number of measurements, i.e. 15 current patterns (each plane in or out of phase with other planes) and 48 electrodes. Therefore the increase in the number of significant singular values is purely due to the amount of information contained and not to a change in the number of measurements.

In order to assess further these sensitivity results, actual images were reconstructed using simulated data, where two spherical anomalies (a single conductor and a single permittivity object) were modeled at the mid-plane of the breast mesh. Images were recovered using each drive pattern. All patterns generated good separation between the two anomalies. Although all of the images have recovered the anomalies in the correct position, results obtained using the first excitation pattern are more blurred. As evident in the results shown in the reconstructed images and table 1, although the peak value reached with the first excitation pattern is slightly higher, the spatial resolution from the second and third excitation patterns is superior. In all cases the third excitation pattern shows the best results, which is consistent with the SVD analysis. It should be noted that the quantitative accuracy of all images is relatively poor which is a common problem in 3D imaging and is sometimes referred to as a partial volume effect that has been reported (Gibson *et al* 2003). The quantitative accuracy can be improved

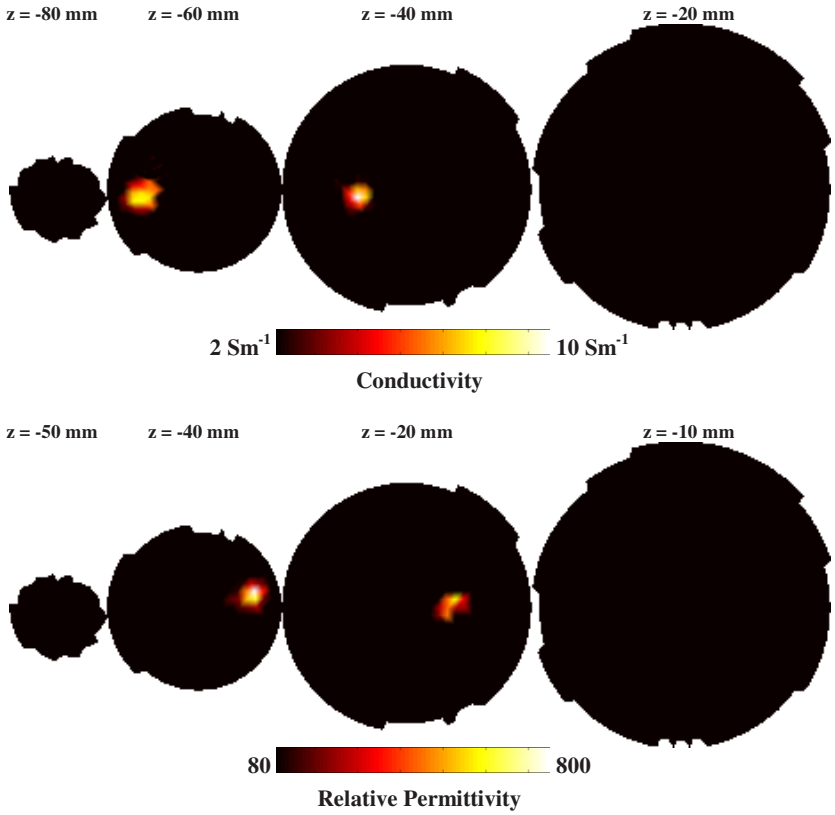

Figure 7. As in figure 4, but using *a priori* information for image reconstruction.

using other types of regularization, reconstruction bases and with the addition of constraints or *a priori* information, as shown in figure 7.

It may be argued that the convergence behavior of the nonlinear reconstruction algorithm is critically related to the choice of the regularization parameter. However, since in all of the results presented here, the initial choice of the regularization parameter and the Levenberg–Marquardt implementation within the nonlinear reconstruction algorithm have been identical regardless of the choice of excitation patterns, it is acceptable to conclude that the difference in the results presented is due to only the choice of the applied excitation patterns. However, it should be again stated that since different current patterns (i.e. in-phase planes versus out-of-phase) will cause the sampling of different volumes, different reconstruction results would be seen if the anomalies are nearer the boundary, but the general trend (that out-of-phase patterns have a higher amount of information) shown here will be expected. The in-phase pattern has shown a slightly better quantitative accuracy, simply because the anomalies are places such that the current flow through the medium is literally sweeping across the medium rather than in between planes of measurement.

6. Conclusions

In this work we have presented our 3D FEM implementation for EIT. We have used this model to assess the benefits of 3 different drive patterns for a female breast model having

4 planes of 16 electrodes. By using singular value decomposition of the Jacobian (sensitivity) matrix, it has been shown that the total amount of information about the domain is increased when phase shift in the z-direction is introduced between the driving patterns spanning the 4 layers of electrodes. Specifically, the best performance was observed when each plane is 90° out-of-phase as relative to the plane above or below it. In order to further investigate these findings, we have also shown reconstructed images from simulated data, which indicate that using out-of-phase driving patterns produces better images in terms of resolution. Furthermore, we have demonstrated 3D image reconstruction at relatively fast computation time and good conductivity/permittivity value separation. Although the quantitative accuracy of the reconstructed images is not yet satisfactory, methods exist for improvement including alternative regularizations, reconstruction bases and use of constraints and/or *a priori* information. An example of *a priori* information used as a parameter reduction technique for image reconstruction has been shown.

The SVD analysis is a powerful method for determining optimal system configurations, which yield the maximum amount of measurement information. For the purpose of the presented study, the three different applied excitation patterns were chosen since these are the obvious extension to the current patterns used for 2D imaging and they are a natural extension to the studies by other researchers in terms of distinguishability (Goble 1990). Further work is needed to assess how different pattern options actually perform in more complex models, for example, in a heterogeneous breast model using different electrode placements. However, regardless of the imaging domain, it has been shown that the SVD method can also be used to optimize a system to achieve the best possible data acquisition from different parts of the imaging domain.

Acknowledgments

This work has been supported by grant NIH P01-CA80139 and by DOD Breast cancer research program DAMD17-03-01-0405.

References

Adler A *et al* 1997 Monitoring changes in lung air and liquid volumes with electrical impedance tomography *J. Appl. Physiol.* **83** 1762–7

Bagshaw A P L, Liston A D, Bayford R H, Tizzard A, Gibson A P, Tidswell A T, Sparkes M K, Dehghani H, Binnie C D and Holder D S 2003 Electrical impedance tomography of human brain function using reconstruction algorithms based on the finite element method *Neuroimage* **20** 752–64

Boone K, Barber D and Brown B 1997 Imaging with electricity: report of the European Concerted Action on Impedance Tomography *J. Med. Eng. Technol.* **21** 201–32

Borsic A 2002 Regularisation methods for imaging from electrical measurements *Thesis* Oxford Brookes University

Brown B H 2003 Electrical impedance tomography (EIT): a review *J. Med. Eng. Technol.* **27** 97–108

Brown B H *et al* 1992 Blood flow imaging using electrical impedance tomography *Clin. Phys. Physiol. Meas.* **13** 175–9

Brown B H *et al* 1994 Multi-frequency imaging and modelling of respiratory related electrical impedance changes *Physiol. Meas.* **15** A1–12

Cherepenin V *et al* 2001 A 3D electrical impedance tomography (EIT) system for breast cancer detection *Physiol. Meas.* **22** 9–18

Dehghani H, Pogue B W, Jiang S, Brooksby B and Paulsen K D 2003 Three dimensional optical tomography: resolution in small object imaging *Appl. Opt.* **42** 3117–28

Erol R A *et al* 1996 Can electrical impedance tomography be used to detect gastro-oesophageal reflux? *Physiol. Meas.* **17** A141–7

Frerichs I 2000 Electrical impedance tomography (EIT) in applications related to lung and ventilation: a review of experimental and clinical activities *Physiol. Meas.* **21** R1–21

Gibson A *et al* 2003 Optical tomography of a realistic neonatal head phantom *Appl. Opt.* **42** 3109–16

Goble J C 1990 The three-dimensional inverse problem in electric current computed tomography *Thesis* Rensselaer Polytechnic Institute

Hoetink A E, Faes Th J C, Marcus J T, Kerkkamp H J J and Heethaar R M 2001 Imaging of thoracic blood volume changes during the heart cycle with electrical impedance using a linear spot-electrode array *IEEE Trans. Med. Imaging* **21** 653–61

Holder D S 1992 Electrical impedance tomography (EIT) of brain function *Brain Topogr.* **5** 87–93

Isaacson D 1986 Distinguishability of conductivities by electric current computed tomography *IEEE Trans. Med. Imaging* **5** 91–5

Kerner T E, Paulsen K D, Hartov A, Soho S K and Poplack S P 2002 Electrical impedance spectroscopy of the breast: clinical results in 26 subjects *IEEE Trans. Med. Imaging* **21** 638–46

Lionheart W R 2004 EIT reconstruction algorithms: pitfalls, challenges and recent developments. *Physiol. Meas.* **25** 125–42

Metherall P *et al* 1996 Three-dimensional electrical impedance tomography *Nature* **380** 509–12

Molinari M *et al* 2002 Comparison of algorithms for non-linear inverse 3D electrical tomography reconstruction *Physiol. Meas.* **23** 95–104

Newell J C, Isaacson D, Saulnier G J, Cheney M and Gisser D G 1993 Acute pulmonary edema assessed by electrical impedance tomography *Proc. Annu. Int. Conf. IEEE Engineering in Medicine and Biology Soc.* 92–3

Noble T J *et al* 1999 Monitoring patients with left ventricular failure by electrical impedance tomography *Eur. J. Heart Failure* **1** 379–84

Polydorides N and Lionheart W R B 2002 A matlab toolkit for three-dimensional electrical impedance tomography: a contribution to the electrical impedance and diffuse optical reconstruction software project *Meas. Sci. Technol.* **13** 1871–83

Polydorides P and McCann M 2002 Electrode configuration for improved spatial resolution in electrical impedance tomography *Meas. Sci. Technol.* **13** 1862–70

Valente Barbas C S 2003 Lung recruitment maneuvers in acute respiratory distress syndrome and facilitating resolution. *Crit. Care Med.* **31** S265–71

van Genderingen H R, van Vught A J and Jansen J R 2003 Estimation of regional lung volume changes by electrical impedance pressures tomography during a pressure–volume maneuver *Intensive Care Med.* **29** 233–40

van Genderingen H R, van Vught A J and Jansen R 2004 Regional lung volume during high-frequency oscillatory ventilation by electrical impedance tomography *Crit. Care Med.* **32** 787–94

Vauhkonen M 1997 Electrical impedance tomography and prior information *Thesis* Univeristy of Kuopio

Vauhkonen P J *et al* 1999 Three-dimensional electrical impedance tomography based on the complete electrode model *IEEE Trans. Biomed. Eng.* **46** 1150–60

Vonk Noordegraaf A *et al* 1997 Noninvasive assessment of right ventricular diastolic function by electrical impedance tomography *Chest* **111** 1222–8

Wang W *et al* 2001 Preliminary results from an EIT breast imaging simulation system *Physiol. Meas.* **22** 39–48

Woo E J *et al* 1992 Measuring lung resistivity using electrical impedance tomography *IEEE Trans. Biomed. Eng.* **39** 756–60

Zou Y and Guo Z 2003 A review of electrical impedance techniques for breast cancer detection *Med. Eng. Phys.* **25** 79–90